Understanding and control of the metallic state in epitaxial NdNiO3

Guo, Qikai

DOI:
10.33612/diss.180302851

Chapter 3

Modulation of the metal-insulator transition in epitaxial nickelates

It is well known that the metal-insulator transition (MIT) that takes place as a function of temperature in the $RENiO_3$ family is highly sensitive to small changes in the structure, caused by external pressure (in bulk materials), epitaxial strain (in thin films) and composition (the choice of rare earth atom). For the work presented in the rest of this thesis, it is of prime importance to be able to synthesize high quality $RENiO_3$ thin films and to achieve control over their properties. Since these materials were not previously investigated in our lab, in this chapter we demonstrate that we are able to grow atomically flat thin films whose properties can be systematically and reproducibly tuned by changing the RE ion, the substrate lattice parameter and orientation and the film thickness. We compare the observed trends with those reported in the literature and, while there is mostly agreement with the existing understanding, we reveal some previously unreported behaviour in the change of the MIT temperature with film thickness.

3.1 Introduction

At a certain temperature, T_{MI}, bulk $RENiO_3$ undergoes a first-order metal-insulator transition, which is associated with a subtle structural change from a high-T orthorhombic phase with crystallographically identical octahedra to a low-T monoclinic phase with alternating large and small octahedra in all main crystallographic axes, adapting to a breathing mode distortion [1–4]. This coupling between electronic and structural properties in nickelates originates from the strong hybridization of the Ni e_{g} orbitals and the O $2p$ orbitals. Instead of a d-d hopping, the electrons in the metallic phase of $RENiO_3$ have been found to hop from O $2p$ orbitals to Ni $3d$ orbitals and leave holes in oxygen atoms [5–9]. $RENiO_3$ is, therefore, classified as a charge-transfer system. Moreover, the charge-transfer energy of this material family is relatively small or even negative, making them very sensitive to the deformation of NiO_6 octahedra, caused by internal or external changes, such as the RE radius and pressure. Recent advances in epitaxial growth of $RENiO_3$ thin films make it possible

to modulate their T_{MI} also by modifying the epitaxial strain, growing the films on different substrates, with added control [9].

An issue that arises from the extreme sensitivity of the transport properties with minute changes in structure and composition is the difficulty to reproduce the exact same resistivity and transition temperature in two different films grown under seemingly identical conditions. This explains the discrepancies in the literature and jeopardizes systematic studies on the effects of a particular parameter. We were initially confronted with these issues until, in discussions with Manuel Bibes, he made us aware of the advantage of using a single phase PLD target to improve reproducibility [10]. This thesis work is based on samples grown from single phase targets, as explained in Chapter 2, and the current chapter is dedicated to demonstrate the achieved control. In the text that follows, we show the effect of different parameters on the resistivity, the temperature of the metal-insulator transition and the sharpness of the transition.

3.2 Experimental methods

In this chapter, three different types of nickelates, including $NdNiO_3$ (NNO), $SmNiO_3$ (SNO), and $Sm_{0.6}Nd_{0.4}NiO_3$ (SNNO), were grown by PLD to study the influence of RE radius on the transport properties. Single-phase target of NNO were obtained from Toshima; while the target of SNNO was made in the labs of Prof. Javier Blasco Carral (CSIC-Universidad de Zaragoza, Spain) and SNO is a homemade target. Single crystals, such as $LaAlO_3$ (LAO), $NdGaO_3$ (NGO), $SrTiO_3$ (STO), $YAlO_3$ (YAO), and $DyScO_3$ (DSO), were employed as the substrates to alter the strain conditions of the films grown on top. Before deposition, all the substrates were thermally annealed and chemically etched to obtain an atomically flat surface with single terminated terraces. The detailed methods for the treatment of different substrates were explained in Chapter 2.

The substrates were heated to a temperature of 700 °C prior to the deposition of the films and were kept at that temperature during growth. Oxygen was present in the growth chamber during deposition with an oxygen pressure of 0.2 mbar and the laser fluence on the target was 2 J/cm^2. After deposition, the samples were cooled down to room temperature at 5 °C/min with a oxygen pressure of 900 mbar. The growth was monitored using Reflection High Energy Electron Diffraction (RHEED). Films with various thicknesses were grown by precisely tuning the deposition time.

For each film, the thicknesses, crystal orientation and phase purity, as well as the epitaxial relation between the film and the substrate, were assessed using X-ray diffraction by means of 2θ-ω scans and reciprocal space maps (RSM), respectively, on a Panalytical, Xpert MRD Pro diffractometer. Cross-sectional specimens of

the films were prepared and studied by scanning transmission electron microscopy (STEM) on a probe corrected FEI Titan 60–300 microscope equipped with a high-brightness field emission gun (X-FEG) and a CEOS aberration corrector for the condenser system. This microscope was operated at 300 kV. High angle annular dark field (HAADF) STEM images were acquired with a convergence angle of 25 mrad and a probe size below 1 Å. The strain state of the films was determined by geometrical phase analysis (GPA) of these HAADF images. The electron microscopy measurement and analyses was performed by César Magén of the Nanotechnology Institute of Aragon (INA) in Spain.

Electrical transport properties were measured between 5 K and 400 K by the van der Pauw method in a Quantum Design Physical Property Measurement System (PPMS), using a Keithley 237 current source and a Agilent 3458A multimeter.

3.3 Results and discussion

3.3.1 Effect of the radius of the rare-earth ion.

In the family of nickelates, $NdNiO_3$ (NNO) and $SmNiO_3$ (SNO) provide very interesting cases to study the influence of RE ionic radius on the properties. Looking at Fig. 1.12, Nd and Sm belong to two different regions of the diagram: with T_{MI}=$T_{Néel}$ and $T_{MI} > T_{Néel}$, respectively[9, 11]. As a consequence, a transition from paramagnetic to antiferromagnetic phase is found in SNO in the insulating region of the phase diagram, while only a single antiferromagnetic arrangement can be expected in the insulating phase of NNO. These distinct behavior of NNO and SNO make them good candidates to study the correlation between electronic and magnetic properties in correlated systems [12]. Moreover, as the T_{MI} of bulk SNO and NNO are symmetrically located on the two sides of room-temperature, the mix of Nd and Sm in nickelates allows to continuously tune the T_{MI} between 200 and 400 K by changing the Nd/Sm ratio [13, 14]. In particular, a room-temperature MIT has been achieved for Sm:Nd= 0.6:0.4 [14–16], and for Sm:Nd=0.5:0.5 in one report[17]).

Here, we prepared three different nickelate film compositions ($Sm_{0.6}Nd_{0.4}NiO_3$ (SNNO), SNO, and NNO) grown on $LaAlO_3$ (LAO) substrates (a substrate that minimizes the amount of strain in epitaxial nickelates) with the same thickness (10 nm) to confirm the reported effect of RE radius on the MIT. Fig. 3.1(a) shows the XRD 2θ-ω scans of the three nickelate compositions around the pseudo-cubic (002) peak. Due to the low thickness of the films and their comparable lattice parameter with the LAO substrate, the diffraction of X-rays by the nickelate films only produces a non-separable shoulder in the left side of the strong substrate peak. However, a tiny shift of the film peak to the high-angle side can still be observed when the RE ion

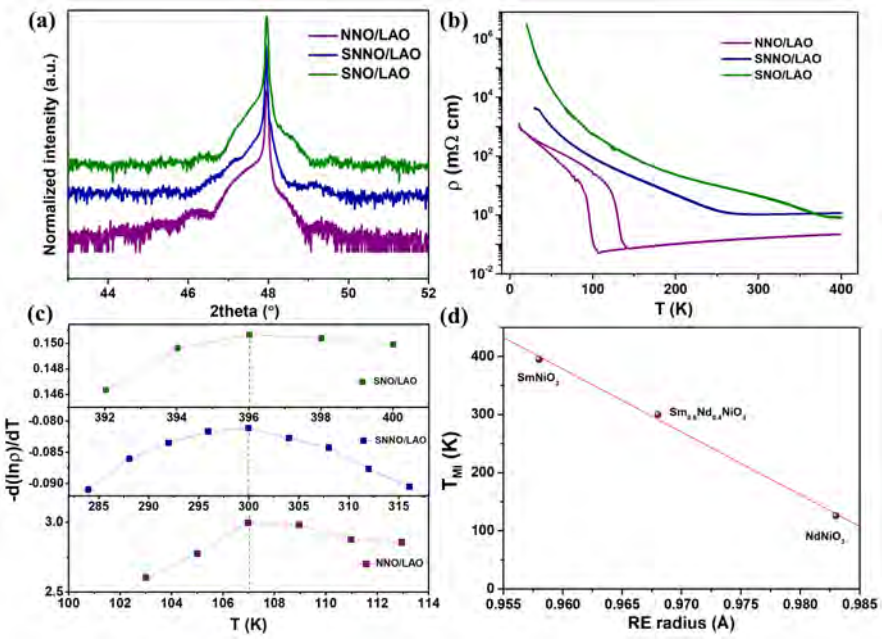

Figure 3.1: *Characterization of three nickelate films with different RE cation ($NdNiO_3$ (NNO), $SmNiO_3$ (SNO), and $Sm_{0.6}Nd_{0.4}NiO_3$ (SSNO)) grown on LAO substrates. (a) XRD 2θ-ω scans around the pseudo-cubic (002) peaks of the substrates, which includes the film peaks. (b) Resistivity as a function of temperature measured in both the cooling and heating runs. (c) The change of sign of the slope of b), represented by -d(lnρ)/dT against T, is used to extract the value of T_{MI}. Note that the T_{MI} of the NNO film is obtained in the data measured during the cooling process. For the other two films no difference between heating and cooling is observed. (d) Evolution of T_{MI} as a function of rare-earth (RE) ionic radius. The RE radius of $Sm_{0.6}Nd_{0.4}NiO_3$ is calculated by considering the weighted average between the two ions. The T_{MI} of the NNO is taken from the average of heating and cooling process. Estimated vertical error bars are smaller than the symbol size for the three data points.*

changes from the larger Nd to the smaller Sm, indicating the expected decrease of the lattice parameter.

The electrical transport properties of the three films are shown in Fig. 3.1b. Clearly, replacing of RE atoms significantly modulates the resistivity and the MIT of these nickelate films. The T_{MI}, the temperature at which the MIT occurs, is determined by a change in the sign of the $\rho(T)$ slope [18, 19]. As shown in Fig. 3.1 (c), the T_{MI} of the NNO/LAO film is about 107 K, while that of SNO/LAO film is as large as to 396 K. This marked change in T_{MI} originates from the different size of A-cations in these two systems. The ionic radii of Nd^{3+} and Sm^{3+} are 0.983 Å and 0.958

Å, respectively. Although the difference of RE radius is only 0.025 Å, it generates a huge difference in T_{MI} of nearly 300 K, indicating a strong electron-lattice coupling in this material family. As we discussed in 1.5.1, the increase of RE size tends to straighten the Ni-O-Ni angle and, consequently, promotes the overlap between Ni-3d and O-2p orbitals, which stabilizes the metallic phase of nickelates. Hence, the T_{MI} of nickelates decreases with increasing RE size.

Following this scenario, the RE atom with radius in between Nd and Sm should give rise to an intermediate T_{MI}, which is confirmed by the SNNO film. In the as-prepared SNNO, the A-sites are occupied by the mixture of Sm and Nd, with an average radius about 0.968 Å (r_{SNNO}=0.6r_{SNO}+0.4r_{NNO}). In this case, the MIT is obtained at 300K. Interestingly, from Fig. 3.1d we found that the decrease of T_{MI} seem to display a linear dependence with the change of ionic radius, which is consistent with the previous works: Ambrosinia $et\ al.$ [14] reported a nearly linear increase of the T_{MI} in $Sm_xNd_{1-x}NiO_3$ from 199 K for x=0 to 378 K for x=1 and achieved a room-temperature MIT for x= 0.6. The linear dependence of T_{MI} with the RE radius emphasizes its dominant role in determining the electronic configurations of nickelates. Note that the difference in the values of T_{MI} for NNO (x=1) and SNO (x=0) between the films reported in the previous work and our present data is attributed to the use of different substrates. NGO substrates were used by Ambrosinia $et\ al.$ and, therefore, their films were subjected to a tensile strain; while the LAO substrates in our work apply a (very small) compressive strain to the films. The effect of strain on the T_{MI} of nickelate films will be discussed in next subsection.

Another significant difference between these three films with different RE cation is that a visible thermal hysteresis is only observed in the NNO/LAO film. Note that hysteresis results from the latent heat required to nucleate one phase into the other and their different thermal dynamics in different directions of the phase transition. Usually, hysteresis is recognized as a property of first-order phase transitions [20]. However, the absence of observable thermal hysteresis in SNO and SNNO cannot be directly interpreted as a signature of second-order phase transition. In fact, the metal-insulator transition in nickelates is considered to be of first-order [21–24]. In the case of the resistivity across metal-insulator transition, the extent of the hysteresis does not directly reflect the coexistence of metallic and insulating phases since metallic resistivity will be observed as soon as a filament of metallic phase percolates though the film. Indeed, a very narrow but recognizable hysteresis of $\rho(T)$ has also been reported in the bulk SNO [25]. The closing of hysteresis in SNO and SNNO films with respect that of NNO films, has been reported to be due to the stronger thermal fluctuations at these higher T_{MI}'s [9, 26, 27]. In addition, recent work on $V_{1-x}W_xO_2$ has shown that the thermal hysteresis can vanish by optimizing the compatibility between the two structures across the phase transition [28].

3.3.2 Effect of the substrate-induced strain.

The stabilization of the high oxidation state of Ni^{3+} in nickelates is an important challenge for studying their electronic and magnetic properties. In the synthesis of bulk $RENiO_3$, the Ni^{3+} state is achieved by performing the solid state reaction under ultra-high oxygen pressure (e.g. 150-200 bars) [18, 29, 30]. Advances in growth technologies, like Magnetron Sputtering (MS) and Pulsed laser deposition (PLD), make it possible to obtain high-quality $RENiO_3$ films by epitaxially growing on single crystalline substrates. In comparison with the solid state method, the epitaxial growth of $RENiO_3$ films not only avoids the application of ultra-high oxygen pressure (i.e. only 0.1-0.2 mbar in PLD) but also, more interestingly, opens a new window for modulating their properties in a controllable way. During the growth, the in-plane lattice parameter of the film is enforced to match the structure of the substrate. Therefore, distinct from its bulk counterpart, the epitaxial film always experiences an in-plane strain ε_{xx}, which can be altered by employing various crystals as substrates. The value of ε_{xx} is evaluated by considering the lattice parameter mismatch between the bulk nickelate of the same composition (a_{bulk}) and the substrate (a_{sub}) as:

$$\varepsilon_{xx} = \frac{a_{sub} - a_{bulk}}{a_{bulk}} \tag{3.1}$$

Next to the epitaxial strain that originates in this way due to the difference in lattice parameters at the growth temperature, additional strains can develop during cooling due to differences in thermal expansion.

In the present work, various substrates with either larger or smaller lattice parameters than bulk NNO were used to generate tensile or compressive strain into the NNO films. The in-plane lattice mismatch of these substrates with bulk NNO is summarized in Fig. 3.2 (a). Among them, the LAO and $YAlO_3$ (YAO) substrates apply a small and large compressive strain on the NNO films, respectively. Whilst the NNO films grown on $NdGaO_3$ (NGO), $SrTiO_3$ (STO) and $DyScO_3$ (DSO) substrates are subjected to an increasingly large tensile strain. By employing these substrates, NNO films with epitaxial strain ranging from -2.9 % to 4.0 % are obtained. Moreover, as a result of the in-plane compressive or tensile strain, the lattice of the films will expand or contract in the out-of-plane direction, correspondingly, to reduce the volume change.

The difference in out-of-plane lattice parameter of films on various substrates was characterized by XRD, by means of 2θ-ω scans around the (002) peak. Due to the ultra-low thickness of NNO films (10 nm), only a weak and broad film peak is observed next to the substrate peak. The calculated (002) peak of the bulk NNO (a_{bulk}=3.808 Å) is marked with a vertical dashed line. NNO films grown on YAO and NGO clearly increase and decrease their out-of-plane lattice, as expected for

compressive and tensile strain, respectively. The films on LAO show a lattice parameter very close to the bulk value, as corresponding to the close lattice matching. However, the films on STO and DSO experience such large lattice mismatch that for the same thickness of 10 nm the films have been relaxed to lattice values close to the bulk. Moreover, as we will discussed in next chapter, oxygen vacancies are prone to be generated in nickelate films under large tensile strain. The creation of oxygen vacancies is well known to expand the lattice of films [31–33] and may also contribute to the relaxation of strain in these largely tensile-strained films.

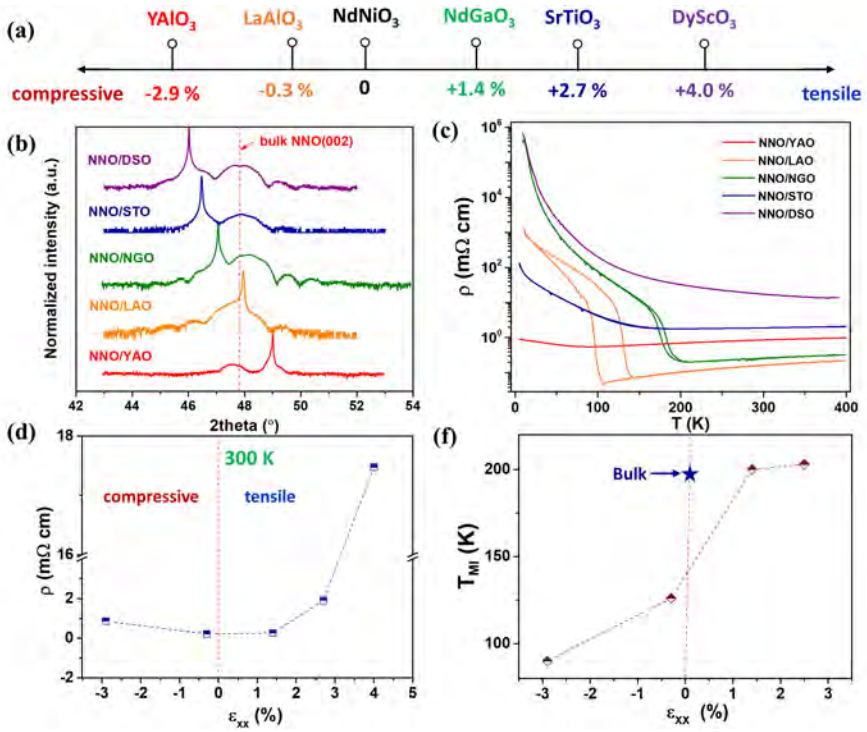

Figure 3.2: *(a) Lattice mismatch between bulk NNO and various substrates. (b) XRD 2θ-ω scan of the (002) peaks of the epitaxial NNO films grown on different substrates. (c) Resistivity of NNO films grown on different substrates as a function of temperature. (d) Room-temperature resistivity against in-plane strain (ε_{xx}) of NNO films. (d) Evolution of T_{MI} as a function of ε_{xx}. The star indicates the T_{MI} of bulk NNO. The T_{MI} of the NNO is taken from the average of heating and cooling process.*

Now we turn our attention to the electrical transport properties of various systems shown in Fig. 3.2 (c). A sharp MIT and visible thermal hysteresis is observed in the two systems (NNO/LAO and NNO/NGO) with lower in-plane strain. While

the hysteresis is fully suppressed in the rest of the films or in films with larger lattice mismatch. As we discussed above, the absence of hysteresis in SNO and SNNO films with higher T_{MI} (above 300 K) are mainly attributed to the stronger thermal fluctuations. However, this scenario may not be appropriate for these NNO films for several reasons: 1) the MIT happens in the NNO/STO film at about 200 K. For the same transition temperature, the bulk NNO and even the NNO/NGO film in the present work display a clear hysteresis; 2) the T_{MI} of NNO/YAO film is lower than 100 K but the hysteresis is still absent; 3) the fully suppressed MIT in NNO/DSO film cannot be explained by the thermal fluctuations. Instead, the strain should play a role, directly or indirectly (via introduction of defects) in determining the closing of the hysteresis here [28]. The dramatic difference between systems with small and large lattice mismatch can also be unveiled by the evolution of resistivity shown in Fig. 3.2(d). The room-temperature resistivity shows an increase with increasing $\varepsilon_{\mathrm{xx}}$ and displays a minimum value when the film has a smallest strain, consistent with the increase in defect content for increasing $\varepsilon_{\mathrm{xx}}$.

It is interesting to note that, by means of local measurements of optical conductivity, Post *et al.* reported that first- and second-order electronic phase transitions are concurrent within the same NNO/NGO film [22]. Specifically, it is proposed by these authors that the first-order transition is followed by the sample bulk, while the second-order transition is found at domain boundaries with enhanced conductivity that appear only during heating, encircling regions of insulating phase. If this is the cause of the decrease in hysteresis in our case still needs to be investigated.

The extracted values of T_{MI} of NNO films grown on various substrates are plotted in Fig. 3.2 (f) as a function of $\varepsilon_{\mathrm{xx}}$. Except for the NNO film on DSO, which experiences an ultra-large tensile strain, all other systems display a transition from metal phase to insulating phase. Among them, the NNO films with tensile strain ($\varepsilon_{\mathrm{xx}} > 0$) have a comparable T_{MI} with that reported in bulk NNO (200 K) [11] and show strain independence. This is consistent with the X-ray observation that the large lattice mismatch leads to a critical thickness for strain relaxation that is lower than the film thickness in this case (10 nm) and, thus, these films are relaxed.

On the contrary, applying compressive strain significantly suppresses the T_{MI} to a value well below that of bulk NNO. This enhanced metallic phase in the compressed systems indicates that the in-plane compressive strain can effectively modify the electronic structure of NNO films. Indeed, as revealed by Density Functional Theory (DFT) calculations, imposing an in-plane compressive constraint to nickelate films results in a straightening of the Ni-O-Ni angle and a stretching of the Ni-O bond length out-of-plane [34]. This decrease of octahedra bending promotes the overlap between Ni $3d$ and O $2p$ orbitals, which broadens the bandwidth and then facilitates the metallic phase, lowering $\mathrm{T_{MI}}$.

Following this scenario, it is natural to suppose that the in-plane tensile strain im-

poses an opposite effect on the T_{MI} of NNO films. Obviously, this is inconsistent with the observations of an unaffected T_{MI} in NNO films with increased tensile strain [9]. As mentioned above, oxygen vacancies, which can expand the lattice, are prone to be formed in the NNO films under nominal tensile strain [35]. As well-known point defects, oxygen vacancies not only increase the scattering of electrons but also cause a localization of electrons in nickelates. Hence, the oxygen-deficiency levels in nickelate films can be directly characterized by the measurement of resistivity. From Fig. 3.2(d), it is clear that the increase of resistivity with $\varepsilon_{\mathrm{xx}}$ is asymmetric and becomes more robust when $\varepsilon_{\mathrm{xx}}>0$. When the tensile strain is too large (see NNO/DSO), the metallic phase of the NNO film is fully suppressed. These phenomena strongly point to a higher oxygen-deficient level in NNO films under tensile strain, as expected. We will discuss this in much detail in the following chapters.

3.3.3 Effect of the substrate orientation

Tunable behaviours of epitaxial NNO films by tailoring the strain emphasize the importance of the substrate. Beyond the mismatch of lattice parameters, the symmetry and orientation of the substrate have also been found to take a noticeable role in modifying the properties of epitaxial films. For example, Moon *et al.* reported an enhanced magnetization and electrical conductivity of $La_{1-x}Sr_xMnO_3$ (LSMO) films grown on cubic substrates compared with those on orthorhombic substrates, despite the same strain state imposed by these substrates [36]. A further work by Chopdekar *et al.* demonstrated that the (001)-oriented STO substrates can suppress the magnetism of LSMO films, while the LSMO films grown on (110)- and (111)-oriented STO maintain the bulk-like magnetism [37]. More interestingly, for nickelates, it was revealed that a polar metallic phase can only be achieved in the NNO films grown on (111)-oriented LAO substrates (caused by the the non-equilibrium octahedral tilt pattern) rather than those with (001) orientation [38]. All this points to a possibility that the substrate orientation can also be used as a tuning knob to modulate the T_{MI} and resistivity of nickelate films.

In the present work, to clarify the pure effect of substrate orientation, several strategies were adopted. Firstly, LAO, which has the smallest mismatch with the nickelates, was employed as the substrate to minimize the influence of strain. Secondly, the thickness of all nickelate films studied here is 5 nm since, as we will discuss in next subsection, the substrate is more likely to imprint its rotation pattern to films below 10 nm. Finally, $RENiO_3$ (RE=Nd, $Sm_{0.6}Nd_{0.4}$, and Sm) with different RE cations were grown to investigate whether the substrate orientation has a comparable influence on systems with different Ni-O-Ni angle.

Fig. 3.3(a) shows the temperature-dependent sheet resistance for NNO films grown on LAO (001) and (111) substrates. Notably, the NNO film grown on (001)-

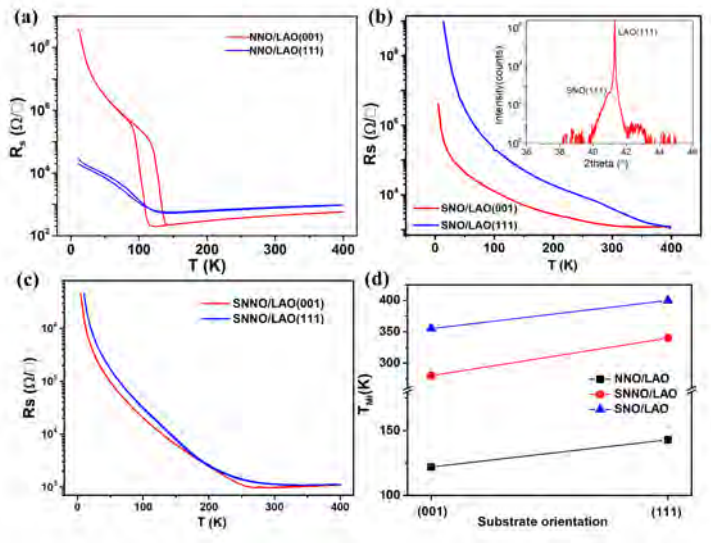

Figure 3.3: *Sheet resistance as a function of temperature for (a) NNO, (b) SNO, and (c) SNNO films grown on (001)- and (111)-oriented LAO substrates, respectively. The thickness is 5 nm for all the films. Inset in (b) shows the 2 theta-omega scanning around LAO(111) peak. (d) Modulation of T_{MI} by substrate orientation in three different nickelate systems.*

oriented LAO undergoes a first-order transition with a sharp MIT and clear thermal hysteresis. However, both the sharpness of the MIT and the size of hysteresis are significantly suppressed for the NNO film grown on (111)-oriented LAO (see inset of Fig. 3.3(b)). For SNO and SNNO films, despite the absence of hysteresis in both orientations, the (111)-oriented substrate still highlight their difference by driving the resistance to a higher value compared with those of (001)-oriented case (see Fig. 3.3(b) and (c)). Another clear difference between nickelate films grown on (001)- and (111)-oriented substrates is observed by the modulation of T_{MI}. As shown in Fig. 3.3 (d), the T_{MI} displays an increase in all of these $RENiO_3$ films when the substrates are changed from LAO(001) to LAO(111). The clear contrast among these films indicates that the orientation of substrate has a fundamental effect on the conductivity of nickelate films.

Both the increase of T_{MI} and resistance in NNO films grown on (111)-oriented LAO with respect to the values observed in (001)-oriented systems reveal a reduced metallicity. Such an orientation driven effect has been reported by Kim *et al.* [38] and Catalano *et al.* [39], manifesting that this puzzling behavior is quite robust in NNO films grown on LAO(111) substrates[39]. The carrier density of NNO film grown on (111)-oriented substrate is also found to be one magnitude less than that

of films with (001)-orientation, which is consistent with lower densities of states near the Fermi level [38].

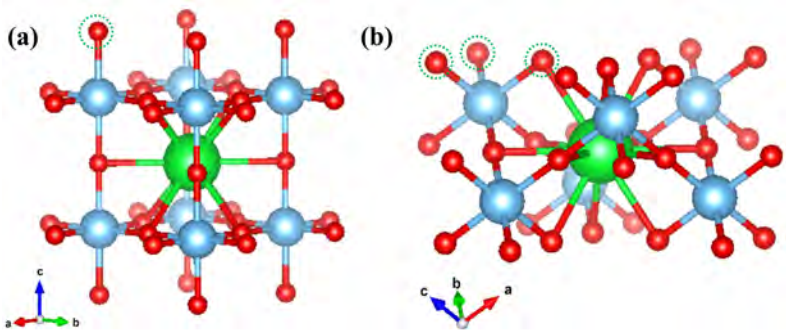

Figure 3.4: *Bond connectivity of heteroepitaxial perovskites along the (111) and (001) orientations. For simplification, a cubic structure is adopted.*

According to Catalano *et al.* [39], the decline of metallic state in NNO films grown on (111)-oriented substrates may arise from an enhanced constraint from the (111) substrates compared with those grown on (001)-oriented substrates. As shown in Fig. 3.4, the (111) orientation permits three bond connections per octahedron (marked with green circles in a cubic structure) in the out-of-plane direction. In vast contrast, the number of bond connections drops to one per octahedron in the (001) orientation. Obviously, the LAO (111) substrate enables a greater control to the NiO_6 rotation patterns [39] and, therefore, has a more robust effect on their electrical properties. However, it is still unclear why the stronger constraint from the LAO(111) substrate can give rise to and increased T_{MI} in NNO films. Note that the LAO exhibits a rhombohedral distortion and a tilt pattern $a^-a^-a^-$, with θ= 174.8°, which is much larger than the Ni–O–Ni angle (157°) in bulk NNO. In this sense, the constraint imposed by the LAO(111) substrate should compel the Ni–O–Ni angle to a larger value towards the Al-O-Al angle, resulting in larger orbital overlap and a lower T_{MI}, contrary with what we observe.

3.3.4 Effect of the film thickness.

As we discussed above, the T_{MI} of NNO films displays a dramatic decrease of more than 100 K when the epitaxial strain is changed from +1.4 % to -2.9 %, demonstrating the robust effect of the strain. However, a continuous modulation of T_{MI} is impossible in this way as only few materials with specific lattice parameters are available to act as the substrate. An alternative method is growing the films on a specific substrate but with different thickness (t). The continuous modulation of strain in the

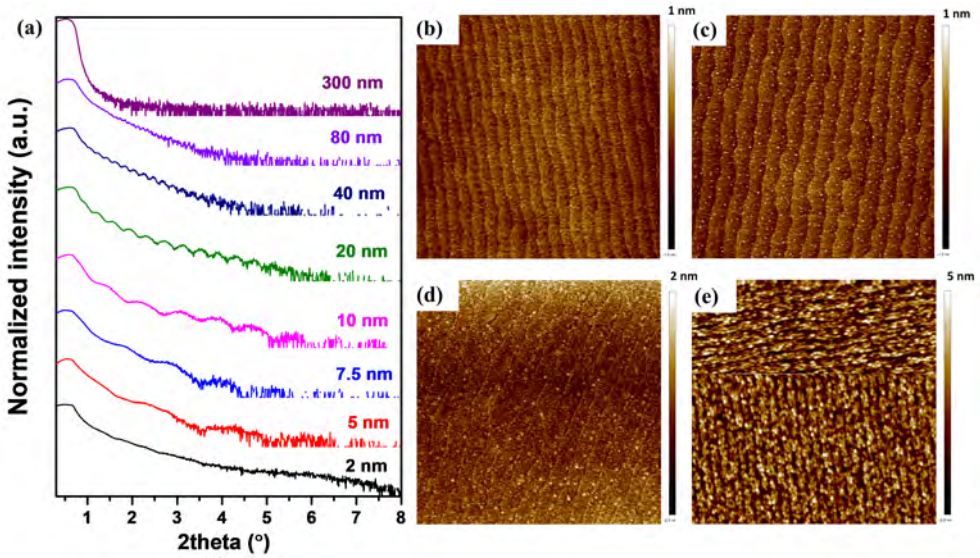

Figure 3.5: *(a) XRD reflectivity of NNO films grown on LAO substrates with different thickness. AFM topography images in a 5×5 μm area in (b) 5 nm, (c) 10 nm, (d) 40 nm, and (e) 300 nm NNO films.*

films is achieved by the gradual relaxation of strain with increasing t. Moreover, a systematic control of t can also help to clarify the influence of interface (for ultra-thin film) and defects (as second phases are more frequently formed in thick films) on the properties of films. Here, NNO films with t ranging from 2 nm to 300 nm were deposited on LAO substrates. The t of each film is determined using x-ray reflectivity (XRR) data shown in Fig. 3.5 (a). Except for the 300 nm film, Kiessing fringes can be observed in all other films, indicating a sharp interface between film and substrate and smooth surface. Moreover, the amplitude of the oscillations shows a visible decrease with increasing t and is fully suppressed in the 300 nm film, which agrees with the expected increasing roughness in thicker films.

The roughness of as-prepared films can also be characterized by Atomic Force Microscopy (AFM). As shown in Fig. 3.5 (b), the topography image of a 5 nm NNO film shows a atomically flat surface and retains the step-and-terrace morphology of the substrate, manifesting the high quality and smaller roughness of the film. However, with the increase of film thickness, small particles start appearing in the 10 nm film (see Fig. 3.5 (c)) and the terraces become less clear in the 40 nm film (Fig. 3.5 (d)). When the film thickness increases to 300 nm (Fig. 3.5 (e)), irregular grains are found to grow along the steps of the substrate and dominate the film morphology. The sharp increase of roughness and the decay of quality in thicker film may arise

from the change of growth mode [40]. At the beginning of the growth, a 2D-like film is epitaxially deposited on the substrate in a layer-by-layer mode, as proven by the RHEED oscillations. At that point, the film is atomically flat and fully coherent with the substrate. However, with further deposition time, the effect of the substrate on the film becomes weaker and weaker, resulting in lattice relaxation by dislocations or other defects in the films. Since then, the roughness of the film increases monotonically with the t and the growth mode change to a "pseudo-2D island growth" [41].

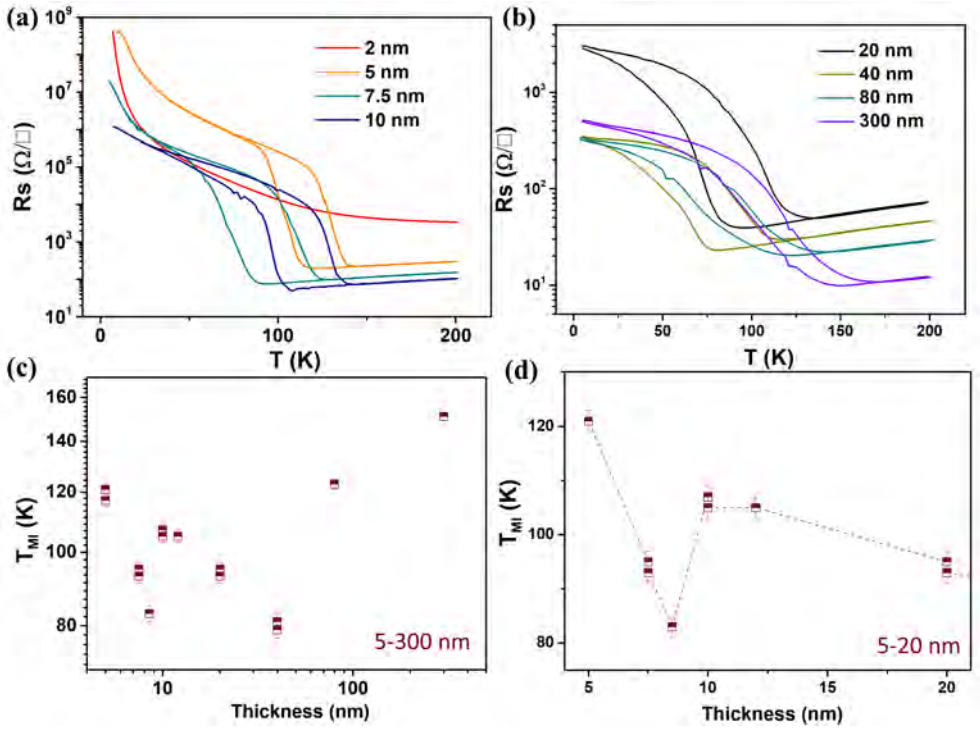

Figure 3.6: *(a) and (b) Sheet resistance of NNO films with different thickness (t) from 2 nm to 300 nm grown on LAO substrates, measured in both the cooling and heating process. (c) Evolution of T_{MI} with the increase of t from 5 nm to 300 nm in log-log mode. (d) T_{MI} $versus$ t in linear plot for films with 5 nm to 20 nm.*

The t dependence of electrical transport properties of these NNO/LAO films are shown in Fig. 3.6. From Fig. 3.6 (a) and (b), it is clear that the sheet resistance of the NNO films shows a continuous decrease with the increasing t, which is consistent with previous works [42–44]. However, different regimes with distinct t-dependence of T_{MI} are observed in Fig. 3.6c. Firstly, the ultra-thin NNO film with only 2 nm dis-

plays an insulating phase in the whole measured temperature range without a MIT. Secondly, for films with t below 40 nm, the further increase of t induces a general decrease of T_{MI}, except for a anomalous dip between 5 nm and 10 nm (see Fig. 3.6 (d)). Note that the growth of multiple films with comparable thickness reproduced this anomalous change of trend. Finally, we observe that for films above 40 nm, the T_{MI} increases with increasing t.

Neglecting, for the time being, the above-mentioned dip for thickness between 5 nm and 10 nm, it is clear the evolution of T_{MI} in NNO/LAO system has a critical thickness, which is around 40 nm in our case. This critical thickness has also been reported in other works but with different values, which may result from the different growth conditions [42, 43]. For instance, Peng $et\ al.$ reported a critical thickness of about 60 u.c. (23 nm) [42], while it decreases to 20 u.c. (8 nm) in the work of Wang $et\ al$ [43]. However, despite these differences, the existence of a critical thickness at which the T_{MI} trend reverses is robust, manifesting a completely different origin of the modulation of T_{MI} in these two regions.

As suggested by previous works [42, 43], the changes at larger thickness are those expected as a result of strain relaxation, while at lower thicknesses the films are below the critical thickness for strain relaxation. Signs of relaxation of strain in thicker films can been observed by various techniques. As shown in Fig. 3.5, the Kiessing fringes start disappearing when the film thickness is above 40 nm, indicating a dramatic increase of film roughness above the critical thickness.

A direct way to reveal the relaxation of strain is performing XRD 2θ-ω scanning and reciprocal space mapping (RSM) of the films. From the data shown in Fig. 3.7 (a), we extract the out-of-plane lattice parameter of films above 20 nm and plot the values as a function of thickness in Fig. 3.7 (b). Note that a reliable out-of-plane lattice parameter of films below 10 nm is difficult to be determined due to the weak XRD intensity and peak broadness. From Fig. 3.7(b), it is obvious that the out-of-plane lattice parameter of films above 40 nm decreases with increasing thickness and gradually approaches the bulk value (marked with dashed line), revealing a strain relaxation in the out-of-plane direction. The relaxation in the in-plane direction was investigated by mapping the selected areas around the off-specular $(103)_{\mathrm{c}}$ peak in reciprocal space. For films below the critical thickness, such as 10 nm (Fig. 3.7(c)) and 40 nm (Fig. 3.7(c)), the K_{par} of the NNO $(103)_{\mathrm{c}}$ peak shows a value identical to that of the LAO substrate (see horizontal lines in the figures), indicating the coherence of film and substrate along the [100] or [010] directions.

However, the center of the film peak shifts to the left of the substrate peak when the thickness is above 40 nm, which is equivalent to an increase of the in-plane lattice parameter. As the NNO films grown on LAO substrate experience an in-plane compressive strain, the increased in-plane lattice parameter in these thicker films, therefore, corresponds to a relaxation of in-plane strain. As we have discussed above, the

application of in-plane compressive strain to nickelate films is always accompanied by an increased Ni-O-Ni angle in the out-of-plane direction. This straightening of the Ni-O-Ni angle induces an enhancement of bandwidth and then drives the T_{MI} down. Conversely, the relaxation of in-plane compressive strain releases the Ni-O-Ni angle to a lower value, approaching to its bulk counterpart, and gives rise to an increased T_{MI} toward 200 K (T_{MI} of bulk NNO). This is consistent with our observation in the films above the critical thickness.

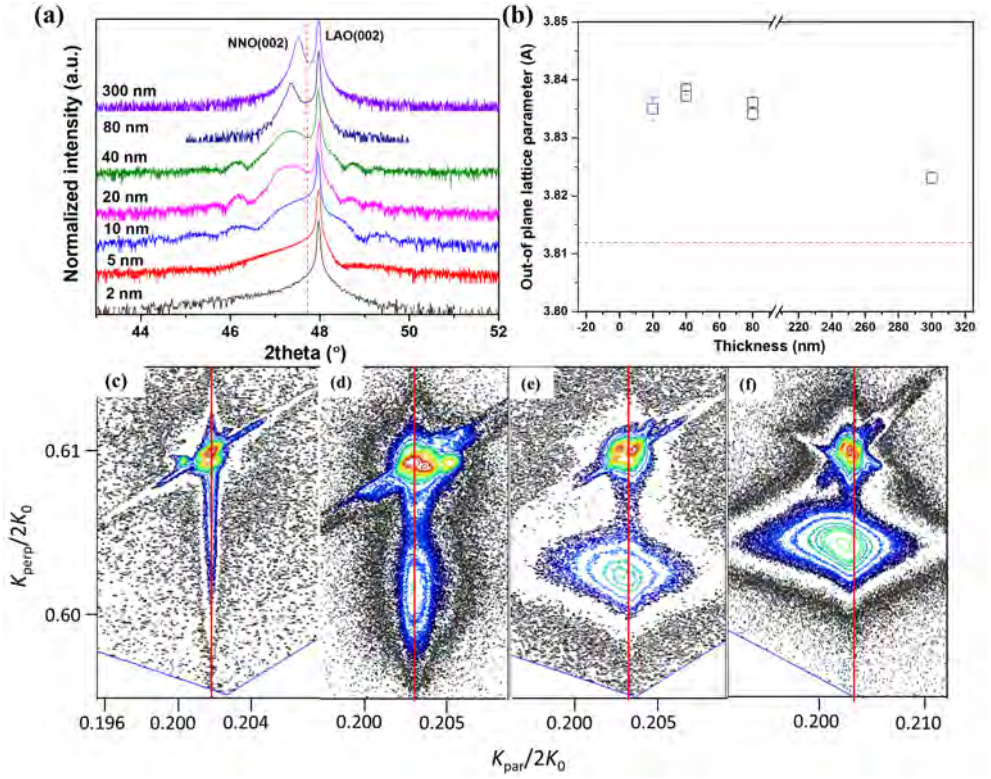

Figure 3.7: *(a) A XRD 2θ-ω scan of the (002) peaks of the epitaxial NNO films with different thickness grown on LAO substrates. (b) The extracted out-of-plane lattice parameters of NNO/LAO films shown in (a) as a function of thickness. The dashed horizontal line indicates the lattice parameter of bulk NNO. The reciprocal space mappings around the $(103)_c$ peak for NNO films with (c) 10 nm, (d) 40 nm, (e) 80 nm, (f) 300 nm. The red solid lines indicate the $K_{par}/2K_0$ of LAO substrate.*

In the "fully strained" regime, below the critical thickness, the observed opposite trend of T_{MI} requires further analysis. As the strain relaxation has been ruled out in this regime, other effects, such as orbital polarization, dimensionality and disorder,

should be considered as candidates to drive the evolution of T_{MI}. In $RENiO_3$, two Ni e_{g} bands with symmetry x^2-y^2 and $3z^2$-r^2 cross the Fermi level. Despite their degeneracy in bulk nickelates, the application of epitaxial strain further breaks symmetry generates an orbital polarization with preference for the x^2-y^2 orbitals in the films with tensile strain and preference for the $3z^2$-r^2 orbitals in the compressive films [44]. By performing X-ray linear dichroism (XLD), Peng *et al.* revealed that this orbital polarization decays with the increase of film thickness even though an obvious strain relaxation is still absent [42]. As the metallic nature of nickelates mainly originates from the overlap of the O $p_{\mathrm{x,y}}$ and Ni x^2-y^2 orbits, the thickness-induced energy lowering of the Ni e_{g} orbitals therefore affects the T_{MI}. For compressive films, the increased thickness is prone to reduce the orbital occupation in the preferred $3z^2$-r^2 orbits. Correspondingly, the occupation in x^2-y^2 orbits will be enhanced, which promotes its overlap with O $p_{\mathrm{x,y}}$ states and drives the T_{MI} toward to a lower temperature.

Thus, on the basis of previous reports, we conclude that the decrease of T_{MI} in films below the critical thickness for strain relaxation mainly arises from the change of orbital polarization (although the cause for this is still an open question), while for films above critical thickness, the gradual strain release is the main cause for the evolution of T_{MI}. However, these origins can not be used to explain the anomalous evolution of T_{MI} in our ultra-thin NNO films (below 10 nm): With the decrease of film thickness, a dimensional crossover from 3D to 2D should occur, emphasizing the importance of surface and interface scattering. Wang *et al.* studied the role of surface effects in determining the electrical behavior of ultra-thin films by capping the NNO films with an insulating LAO layer [43]. They found the suppressed metallic nature of ultra-thin films can be recovered in this way. This revealed that surface scattering dominates the electrical properties of ultra-thin films, which we expect is what happens in our 2 nm NNO films.

Now the only observation which is still not clear is the anomalous dip between 5 nm and 10 nm. To clarify this behaviour, scanning transmission electron microscopy (STEM) was performed to characterize the microstructure of NNO films. The STEM images shown in Fig. 3.8 (a) and (d) indicate a cube-on-cube growth of both 5 nm and 10 nm NNO films on LAO substrates, with atomically sharp interfaces. The octahedra tilt patterns in the selected regions (marked with yellow square) were investigated by a Fast Fourier Transform (FFT) analyses, as shown in Fig. 3.8 (b) and (e) for 5 nm and 10 nm NNO films, respectively.

Interestingly, we found a set of half integer reflections (marked with yellow circles) present in the 10 nm film; while these reflections are absent for 5 nm film. Similar half-order spots were also reported by Kim *et al.* and were attributed to the in-phase c^+ octahedra rotations in the orthorhombic ($Pbnm$, $a^-a^-c^+$) phases of NNO [38]. Correspondingly, it is natural to suppose that the absence of these half integer

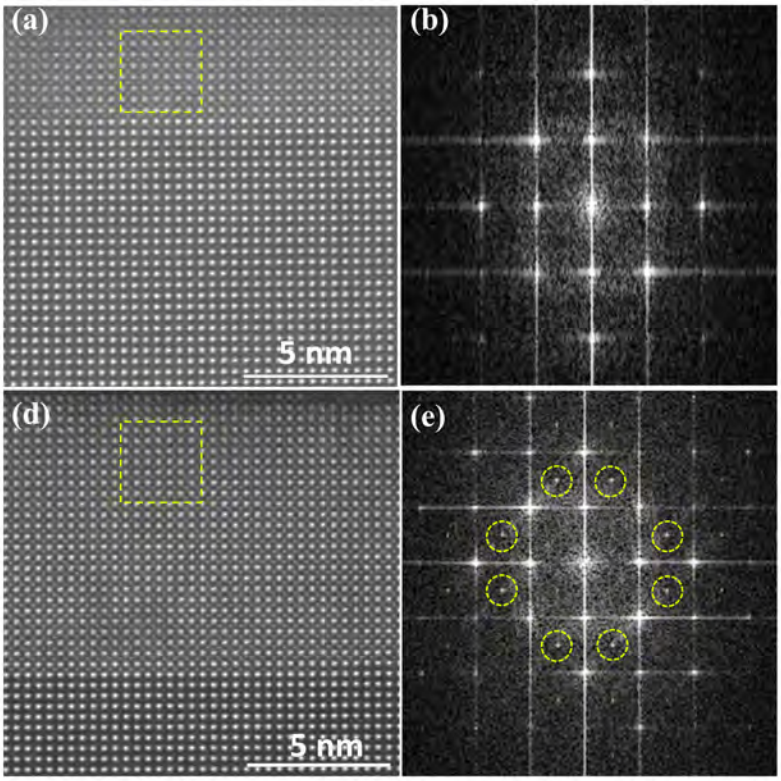

Figure 3.8: *STEM images of (a) 5 nm and (b) 10 nm NNO/LAO films. (c) and (d) show the Fast Fourier transform (FFT) of the selected regions (yellow rectangles) in (a) and (b), respectively. The dotted yellow circles represent half-order spots, which usually come from the oxygen octahedral rotations.*

reflections in the 5 nm NNO film manifests the suppression of the c^+ octahedra tilt pattern in ultra-thin NNO films. The suppression of c^+ octahedra rotation was also observed by Chen $et\ al$ in NNO/STO superlattices [45], although in their case the effect is observed for smaller thicknesses: an unexpected decline of T_{MI} was observed by these authors when the thickness of the NNO layers was decreased from 6 unit cells (uc) to 5 uc.

Note that these half-order peaks are also absent in the rhombohedral ($R\bar{3}c$, $a^-a^-a^-$) LAO substrate. Therefore, it is likely that the LAO substrate only imprints its characteristic rotation pattern of AlO_6 octahedra up to a certain depth into the films; while the bulk equilibrium $a^-a^-c^+$ tilt recovers for films above this (second) critical thickness. As the electronic configuration of nickelates is very sensitive to the octahedra

tilts, the suppressed in-phase c^+ rotations could be responsible for their anomalous drop of T_{MI} in our NNO films between 5 nm and 10 nm.

In addition, it is interesting to consider the effects of a possible electronic reconstruction at the NNO/LAO interface in the ultra-thin films ($e.g$ several unit cells) [46, 47]. As pointed out by Liu $et\ al.$, despite of having the same valence, the electronegativity of Al is much lower compared to that of Ni and, therefore, the formed Ni-O-Al bond at the interface is also less covalent than the normal Ni-O-Ni bond. Moreover, the d-electron states, which are crucial in determining the electronic configuration of Ni, are absent on Al. Both of these effects lead to a significant suppression of ligand hole density on the apical Oxygen. However, we expect that any effect of a LAO-induced electronic reconstruction would only affect the first atomic layers; while the anomalous behaviour in the T_{MI} trend observe in our films reaches more than 20 atomic layers. Instead, the observed suppression of octahedral rotation in the films below 8.5 nm and the additional effect of surface scattering may explain the anomalous dip in the evolution of T_{MI}, added to the overall effect exerted by the orbital polarization.

3.4 Conclusion

To conclude, we have been able to grow high quality nickelate films with different compositions, thicknesses and strain state in a systematic manner, reproducing previously reported trends (some still unexplained) and revealing some unreported behaviour, such as the existence of a narrow thickness range, between 6 nm and 9 nm, in which the T_{MI} is anomalously reduced. This prepares us for an in-depth investigation of the role of disorder in the following chapters.

Bibliography

[1] J. Alonso, J. García-Muñoz, M. Fernández-Díaz, M. Aranda, M. Martínez-Lope, and M. Casais, "Charge disproportionation in $RNiO_3$ perovskites: Simultaneous metal-insulator and structural transition in $YNiO_3$," *Physical review letters* **82**(19), p. 3871, 1999.

[2] J. Alonso, M. Martínez-Lope, M. Casais, J. García-Muñoz, and M. Fernández-Díaz, "Room-temperature monoclinic distortion due to charge disproportionation in $RNiO_3$ perovskites with small rare-earth cations (R=Ho, Y, Er, Tm,Yb,and Lu): A neutron diffraction study," *Physical Review B* **61**(3), p. 1756, 2000.

[3] M. Medarde, M. Fernández-Díaz, and P. Lacorre, "Long-range charge order in the low-temperature insulating phase of $PrNiO_3$," *Physical Review B* **78**(21), p. 212101, 2008.

[4] J. García-Muñoz, M. Aranda, J. Alonso, and M. Martínez-Lope, "Structure and charge order in the antiferromagnetic band-insulating phase of $NdNiO_3$," *Physical Review B* **79**(13), p. 134432, 2009.

[5] R. J. Green, M. W. Haverkort, and G. A. Sawatzky, "Bond disproportionation and dynamical charge fluctuations in the perovskite rare-earth nickelates," *Physical Review B* **94**(19), p. 195127, 2016.

[6] S. Johnston, A. Mukherjee, I. Elfimov, M. Berciu, and G. A. Sawatzky, "Charge disproportionation without charge transfer in the rare-earth-element nickelates as a possible mechanism for the metal-insulator transition," *Physical review letters* **112**(10), p. 106404, 2014.

[7] V. Bisogni, S. Catalano, R. J. Green, M. Gibert, R. Scherwitzl, Y. Huang, V. N. Strocov, P. Zubko, S. Balandeh, J.-M. Triscone, *et al.*, "Ground-state oxygen holes and the metal–insulator transition in the negative charge-transfer rare-earth nickelates," *Nature Communications* **7**(1), pp. 1–8, 2016.

[8] S. Middey, J. Chakhalian, P. Mahadevan, J. Freeland, A. J. Millis, and D. Sarma, "Physics of ultrathin films and heterostructures of rare-earth nickelates," *Annual Review of Materials Research* **46**, pp. 305–334, 2016.

[9] S. Catalano, M. Gibert, J. Fowlie, J. Iniguez, J.-M. Triscone, and J. Kreisel, "Rare-earth nickelates $RNiO_3$: thin films and heterostructures," *Reports on Progress in Physics* **81**(4), p. 046501, 2018.

[10] D. Preziosi, A. Sander, A. Barthélémy, and M. Bibes, "Reproducibility and off-stoichiometry issues in nickelate thin films grown by pulsed laser deposition," *AIP Advances* **7**(1), p. 015210, 2017.

[11] J. Torrance, P. Lacorre, A. Nazzal, E. Ansaldo, and C. Niedermayer, "Systematic study of insulator-metal transitions in perovskites $RNiO_3$ (R= Pr, Nd, Sm, Eu) due to closing of charge-transfer gap," *Physical Review B* **45**(14), p. 8209, 1992.

[12] I. Vobornik, L. Perfetti, M. Zacchigna, M. Grioni, G. Margaritondo, J. Mesot, M. Medarde, and P. Lacorre, "Electronic-structure evolution through the metal-insulator transition in $RNiO_3$," *Physical Review B* **60**(12), p. R8426, 1999.

[13] G. Frand, O. Bohnke, P. Lacorre, J. Fourquet, A. Carré, B. Eid, J. Théobald, and A. Gire, "Tuning of metal/insulator transition around room temperature of perovskites $Sm_{1-x}Nd_xNiO_3$," *Journal of Solid State Chemistry* **120**(1), pp. 157–163, 1995.

[14] A. Ambrosini and J.-F. Hamet, "$Sm_{1-x}Nd_xNiO_3$ thin-film solid solutions with tunable metal–insulator transition synthesized by alternate-target pulsed-laser deposition," *Applied physics letters* **82**(5), pp. 727–729, 2003.

[15] C. Girardot, J. Kreisel, S. Pignard, N. Caillault, and F. Weiss, "Raman scattering investigation across the magnetic and metal-insulator transition in rare earth nickelate $RNiO_3$ (R= Nd, Sm) thin films," *Physical Review B* **78**(10), p. 104101, 2008.

[16] H. Huang, Z. Luo, Y. Yang, M. Yang, H. Wang, G. Pan, Y. Lu, and C. Gao, "The effect of growth oxygen pressure on the metal-insulator transition of ultrathin $Sm_{0.6}Nd_{0.4}NiO_{3-\delta}$ epitaxial films," *RSC Advances* **4**(98), pp. 55082–55086, 2014.

[17] X. Lian, F. Chen, X. Tan, L. Wang, X. Xuan, G. Gao, S. Jin, and W. Wu, "Controlling the sharpness of room-temperature metal-insulator transition in epitaxial $Sn_{0.5}Nd_{0.5}NiO_3$ films," *AIP Advances* **3**(6), p. 062133, 2013.

[18] P. Canfield, J. Thompson, S.-W. Cheong, and L. Rupp, "Extraordinary pressure dependence of the metal-to-insulator transition in the charge-transfer compounds $NdNiO_3$ and $PrNiO_3$," *Physical review B* **47**(18), p. 12357, 1993.

[19] G. Catalan, R. Bowman, and J. Gregg, "Metal-insulator transitions in $NdNiO_3$ thin films," *Physical Review B* **62**(12), p. 7892, 2000.

[20] G. Catalan, "Progress in perovskite nickelate research," *Phase Transitions* **81**(7-8), pp. 729–749, 2008.

[21] G. Mattoni, P. Zubko, F. Maccherozzi, A. J. van der Torren, D. B. Boltje, M. Hadjimichael, N. Manca, S. Catalano, M. Gibert, Y. Liu, *et al.*, "Striped nanoscale phase separation at the metal–insulator transition of heteroepitaxial nickelates," *Nature communications* **7**(1), pp. 1–7, 2016.

[22] K. Post, A. McLeod, M. Hepting, M. Bluschke, Y. Wang, G. Cristiani, G. Logvenov, A. Charnukha, G. Ni, P. Radhakrishnan, *et al.*, "Coexisting first-and second-order electronic phase transitions in a correlated oxide," *Nature Physics* **14**(10), pp. 1056–1061, 2018.

[23] D. Preziosi, L. Lopez-Mir, X. Li, T. Cornelissen, J. H. Lee, F. Trier, K. Bouzehouane, S. Valencia, A. Gloter, A. Barthélémy, *et al.*, "Direct mapping of phase separation across the metal–insulator transition of $NdNiO_3$," *Nano letters* **18**(4), pp. 2226–2232, 2018.

[24] B. Mundet, C. Domínguez, J. Fowlie, M. Gibert, J.-M. Triscone, and D. T. Alexander, "Near-atomic-scale mapping of electronic phases in rare earth nickelate superlattices," *Nano Letters* , 2021.

[25] J. Pérez-Cacho, J. Blasco, J. García, M. Castro, and J. Stankiewicz, "Study of the phase transitions in," *Journal of Physics: Condensed Matter* **11**(2), p. 405, 1999.

[26] X. Granados, J. Fontcuberta, X. Obradors, and J. Torrance, "Metastable metallic state and hysteresis below the metal-insulator transition in $PrNiO_3$," *Physical Review B* **46**(24), p. 15683, 1992.

[27] X. Granados, J. Fontcuberta, X. Obradors, L. Manosa, and J. Torrance, "Metallic state and the metal-insulator transition of $NdNiO_3$," *Physical Review B* **48**(16), p. 11666, 1993.

[28] Y. Liang, S. Lee, H. Yu, H. Zhang, Y. Liang, P. Zavalij, X. Chen, R. James, L. Bendersky, A. Davydov, *et al.*, "Tuning the hysteresis of a metal-insulator transition via lattice compatibility," *Nature communications* **11**(1), pp. 1–8, 2020.

[29] G. Demazeau, A. Marbeuf, M. Pouchard, and P. Hagenmuller, "Sur une série de composés oxygènes du nickel trivalent derivés de la perovskite," *Journal of Solid State Chemistry* **3**(4), pp. 582–589, 1971.

[30] P. Lacorre, J. Torrance, J. Pannetier, A. Nazzal, P. Wang, and T. Huang, "Synthesis, crystal structure, and properties of metallic $PrNiO_3$: Comparison with metallic $NdNiO_3$ and semiconducting $SmNiO_3$," *J. Solid State Chem* **91**(2), pp. 225–237, 1991.

[31] L. López-Conesa, J. M. Rebled, D. Pesquera, N. Dix, F. Sánchez, G. Herranz, J. Fontcuberta, C. Magén, M. J. Casanove, S. Estradé, *et al.*, "Evidence of a minority monoclinic $LaNiO_{2.5}$ phase in lanthanum nickelate thin films," *Physical Chemistry Chemical Physics* **19**(13), pp. 9137–9142, 2017.

[32] R. U. Chandrasena, W. Yang, Q. Lei, M. U. Delgado-Jaime, K. D. Wijesekara, M. Golalikhani, B. A. Davidson, E. Arenholz, K. Kobayashi, M. Kobata, *et al.*, "Strain-engineered oxygen vacancies in $CaMnO_3$ thin films," *Nano letters* **17**(2), pp. 794–799, 2017.

[33] F. Conchon, A. Boulle, R. Guinebretière, C. Girardot, S. Pignard, J. Kreisel, F. Weiss, E. Dooryhee, and J.-L. Hodeau, "Effect of tensile and compressive strains on the transport properties of $SmNiO_3$ layers epitaxially grown on (001) $SrTiO_3$ and $LaAlO_3$ substrates," *Applied Physics Letters* **91**(19), p. 192110, 2007.

[34] S. Catalano, M. Gibert, V. Bisogni, O. Peil, F. He, R. Sutarto, M. Viret, P. Zubko, R. Scherwitzl, A. Georges, *et al.*, "Electronic transitions in strained $SmNiO_3$ thin films," *APL materials* **2**(11), p. 116110, 2014.

[35] F. Conchon, A. Boulle, R. Guinebretière, E. Dooryhee, J.-L. Hodeau, C. Girardot, S. Pignard, J. Kreisel, F. Weiss, L. Libralesso, *et al.*, "Investigation of strain relaxation mechanisms and transport properties in epitaxial $SmNiO_3$ films," *Journal of Applied Physics* **103**(12), p. 123501, 2008.

[36] E. Moon, P. Balachandran, B. J. Kirby, D. Keavney, R. Sichel-Tissot, C. Schleputz, E. Karapetrova, X. Cheng, J. M. Rondinelli, and S. May, "Effect of interfacial octahedral behavior in ultrathin manganite films," *Nano letters* **14**(5), pp. 2509–2514, 2014.

[37] R. V. Chopdekar, E. Arenholz, and Y. Suzuki, "Orientation and thickness dependence of magnetization at the interfaces of highly spin-polarized manganite thin films," *Physical Review B* **79**(10), p. 104417, 2009.

[38] T. Kim, D. Puggioni, Y. Yuan, L. Xie, H. Zhou, N. Campbell, P. Ryan, Y. Choi, J.-W. Kim, J. Patzner, *et al.*, "Polar metals by geometric design," *Nature* **533**(7601), pp. 68–72, 2016.

[39] S. Catalano, M. Gibert, V. Bisogni, F. He, R. Sutarto, M. Viret, P. Zubko, R. Scherwitzl, G. Sawatzky, T. Schmitt, *et al.*, "Tailoring the electronic transitions of $NdNiO_3$ films through (111) pc oriented interfaces," *APL materials* **3**(6), p. 062506, 2015.

[40] C. Daumont, D. Mannix, S. Venkatesan, G. Catalan, D. Rubi, B. Kooi, J. T. M. De Hosson, and B. Noheda, "Epitaxial $TbMnO_3$ thin films on $SrTiO_3$ substrates: a structural study," *Journal of Physics: Condensed Matter* **21**(18), p. 182001, 2009.

[41] J. Shin, S. V. Kalinin, A. Y. Borisevich, E. W. Plummer, and A. P. Baddorf, "Layer-by-layer and pseudo-two-dimensional growth modes for heteroepitaxial $BaTiO_3$ films by exploiting kinetic limitations," *Applied Physics Letters* **91**(20), p. 202901, 2007.

[42] J. Peng, C. Song, M. Wang, F. Li, B. Cui, G. Wang, P. Yu, and F. Pan, "Manipulating the metal-to-insulator transition of $NdNiO_3$ films by orbital polarization," *Physical Review B* **93**(23), p. 235102, 2016.

[43] L. Wang, S. Ju, L. You, Y. Qi, Y.-w. Guo, P. Ren, Y. Zhou, and J. Wang, "Competition between strain and dimensionality effects on the electronic phase transitions in $NdNiO_3$ films," *Scientific reports* **5**, p. 18707, 2015.

[44] E. Mikheev, A. J. Hauser, B. Himmetoglu, N. E. Moreno, A. Janotti, C. G. Van de Walle, and S. Stemmer, "Tuning bad metal and non-Fermi liquid behavior in a Mott material: Rare-earth nickelate thin films," *Science advances* **1**(10), p. e1500797, 2015.

[45] B. Chen, N. Gauquelin, R. J. Green, J. H. Lee, C. Piamonteze, M. Spreitzer, D. Jannis, J. Verbeeck, M. Bibes, M. Huijben, *et al.*, "Spatially controlled octahedral rotations and metal–insulator transitions in nickelate superlattices," *Nano letters* **21**(3), pp. 1295–1302, 2021.

[46] J. Liu, S. Okamoto, M. Van Veenendaal, M. Kareev, B. Gray, P. Ryan, J. Freeland, and J. Chakhalian, "Quantum confinement of mott electrons in ultrathin $LaNiO_3/LaAlO_3$ superlattices," *Physical Review B* **83**(16), p. 161102, 2011.

[47] A. S. Disa, A. B. Georgescu, J. L. Hart, D. P. Kumah, P. Shafer, E. Arenholz, D. A. Arena, S. Ismail-Beigi, M. L. Taheri, F. J. Walker, *et al.*, "Control of hidden ground-state order in $NdNiO_3$ superlattices," *Physical Review Materials* **1**(2), p. 024410, 2017.